Available online at https://link.springer.com/journal/42241
http://www.jhydrodynamics.com
Journal of Hydrodynamics, 2020, 32(5): 865-878
https://doi.org/10.1007/s42241-020-0060-y

Numerical investigations of the transient cavitating vortical flow structures over a flexible NACA66 hydrofoil *

Ren-fang Huang, Te-zhuan Du, Yi-wei Wang, Cheng-guang Huang
Key Laboratory for Mechanics in Fluid Solid Coupling Systems, Institute of Mechanics, Chinese Academy of Sciences, Beijing 100190, China

(Received, Revised August 20, 2019, Accepted October 14, 2019, Published online October 28, 2019, Published online October 29, 2020)

Abstract: In this paper, the cavitating flow over a flexible NACA66 hydrofoil is studied numerically by a modified fluid-structure interaction strategy with particular emphasis on understanding the flow-induced vibration and the cavitating vortical flow structures. The modified coupling approaches include (1) the hydrodynamic solution obtained by the large eddy simulation (LES) together with a homogenous cavitation model, (2) the structural deformation solved with a cantilever beam equation, (3) fluid-structural interpolation and volume mesh motion based on the radial basis functions and greedy algorithm. For the flexible hydrofoil, the dominant flow-induced vibration frequency is twice of the cavity shedding frequency. The cavity shedding frequency is same for the rigid and flexible hydrofoils, demonstrating that the structure vibration is not large enough to affect the cavitation evolution. The predicted cavitating behaviors are strongly three-dimensional, that is, the cavity is (a) of a triangular shape near the hydrofoil tip, (b) of a rectangular shape near the hydrofoil root, and (c) with a strong unsteadiness in the middle of the span, including the attached cavity growth, oscillation and shrinkage, break-off and collapse downstream. The unsteady hydroelastic response would strongly affect the cavitation shedding process with small-scale fragments at the cavity rear part. Furthermore, three vortex identification methods (i.e., the vorticity, the Q- criteria and the Ω method) are adopted to investigate the cavitating vortex structures around the flexible hydrofoil. It is indicated that the cavity variation trend is consistent with the vortex evolution. The vortex structures are distributed near the foil trailing edge and in the cavitation region, especially at the cavity-liquid interface. With the transporting downstream the shedding cavities, the vortices gradually increase in the wake flows.

Key words: Cloud cavitation, flexible hydrofoil, Ω method, flow-induced vibration

Introduction

The cavitation occurs when the local pressure drops below the liquid saturation vapor pressure. It is a common phenomenon in water turbines, marine vehicles, propellers and valves, etc. The cavitation oscillation, break-off and collapse process may cause many problems such as the pressure pulsation, the structural vibration, the noise and the surface erosion. Due to its importance in a wide range of fundamental studies and engineering applications, the studies of the cavitation dynamics were comprehensively reviewed in literature[1-4]. Due to the cavitation unsteadiness including the cavity breakdown and collapse, strong instantaneous loads will be produced, causing further hydrodynamic instabilities, even structural failures. Meanwhile, the flow-induced vibration will in turn affect the transient cavitating flows. Therefore, it is of great significance to investigate the flow-induced vibrations in unsteady cavitating flows.

Many experiments[5-7] and numerical simulations[8-10] were conducted to study the cavitation dynamics and the related structure vibrations. Amromin and Kovinskaya[11] analyzed the vibrations of an elastic wing in an attached cavitating flows, with the wing vibration solved based on the beam equation,. It is indicated that the high-frequency band of a significant vibration is related with the elastic resonance and the low-frequency band corresponds to the cavity-volume oscillations governed by the cavity length-based Strouhal number.

With the measurements of the displacements on the free foil tip section using a high speed video camera and the surface velocity vibrations using a Doppler vibrometer, Ducoin et al.[7] studied the

* Project supported by the National Natural Science Foundation of China (Grant Nos. 11772340, 11872065).
Biography: Ren-fang Huang (1990-), Female, Ph. D., Assistant Professor, E-mail: hrenfang@yeah.net
Corresponding author: Te-zhuan Du,
E-mail: dutezhuan@imech.ac.cn

fluid-structure interaction on a rectangular cantilevered flexible hydrofoil in the cavitating flows and found that the cavitation greatly increases the vibration level due to the hydrodynamic loading unsteadiness and the change of the modal responses of specific frequencies. Wu et al.[6, 8, 12] investigated the cavitating flow-induced vibrations of a flexible NACA66 hydrofoil through both experiments and numerical simulations, and it was found that the maximum vibration amplitude keeps relatively small for the inception and sheet cavitation, it increases dramatically for the cloud cavitation and declines for the supercavitation. De La Torre et al.[13] conducted a large range of experiments for a two-dimensional NACA0009 truncated hydrofoil submerged in the air, the still water and in various cavitation regimes, and a linear correlation was found between the added mass and the entrained mass related to the cavity, including the density, the dimension and the location relative to the specific modal shape deformation. Smith et al.[5] experimentally measured the cloud cavitation behaviors around the NACA0009 hydrofoil, and it is demonstrated that the hydrofoil compliance would damp the high frequency force fluctuations and is closely associated with the normal force and the tip deflection. With focus on the effects of the cavitation and the fluid-structure interaction on the mechanism of the vortex generation, Ausoni et al.[14] found that the vortex shedding frequency increases up to 15% in a fully developed cavitation and the cavitation onset will significantly increase the vortex-induced vibration level due to the increase of the vorticity caused by the cavitation. For the cross flow around a two-dimensional elastic cylinder, So et al.[15] investigated the free vibrations and their effects on the near wake flows by using a laser vibrometer to measure the bending displacements and a laser Doppler anemometer to measure the velocities. It was shown that the cylinder vibrations have little or no effect on the mean drag and the normalized mean field, but they enhance the turbulent mixing, with a substantial increase of the turbulent intensities. The studies of Ausoni et al.[14] and So et al.[15], indicated that the structure vibration is closely associated with the large-scale vortical motion. Moreover, the cavitation would promote the vortex production with the contributions from the vortex stretching, the vortex dilatation and the baroclinic torque terms[16-17].

The accurate vortex identification is essential for better understanding the structural vibration characteristics and the transient cavitation patterns, as well as the vortex dynamics. There are various traditional vortex visualization methods including the λ_2 method[18], the Q- criterion[19], and the Lagrange method[20-21]. Generally speaking, the λ_2 method and the Q- criterion involve the subjective selection of a threshold for the vortex visualization, varying from case to case and with no universally acknowledged guidelines. In view of these problems, Liu and his collaborators recently proposed new vortex identification methods, that is, the Ω method[22] and the Liutex/Rortex[22]. Zhang et al.[23] reviewed various vortex identification methods with applications of the wake flow around the moving bodies, the atmosphere boundary layer and the reversible pump turbine. It is found that the Ω method is superior to other methods when $\Omega = 0.52$, as is recommended to define the vortex boundary. Different vortex identification methods were used by Wang et al.[24] to study the cavitation vortex dynamics in the unsteady sheet/cloud cavitating flows with shock waves, indicating that different methods can identify vortices in different cavitation regions. However, there are few studies about the application of the Ω method and the Q- criterion to the cavitating flow with consideration of the fluid-structure interaction.

1. Numerical approach

1.1 *Governing equations*

The unsteady Navier-Stokes equations are solved by using the large eddy simulation (LES) method and a mass transfer cavitation model. In the homogenous framework, the vapor/liquid fluid components are assumed to share the same velocity and pressure fields. The basic governing equations consist of the mass and momentum conservation equations.

$$\frac{\partial \rho}{\partial t} + \frac{\partial (\rho u_j)}{\partial x_j} = 0 \tag{1}$$

$$\frac{\partial (\rho u_i)}{\partial t} + \frac{\partial (\rho u_i u_j)}{\partial x_j} = -\frac{\partial p}{\partial x_i} + \frac{\partial}{\partial x_j}\left(\mu \frac{\partial u_i}{\partial x_j}\right) \tag{2}$$

where u_i is the velocity component in the i direction, p is the pressure and the laminar viscosity μ and the mixture density ρ are defined as

$$\mu = (1-\alpha_v)\mu_l + \alpha_v \mu_v \tag{3}$$

$$\rho = (1-\alpha_v)\rho_l + \alpha_v \rho_v \tag{4}$$

where α is the volume fraction of the different phases and the subscripts l and v represent the liquid water and the water vapor, respectively.

The vapor volume fraction α_v is governed by the cavitation model developed by Schnerr and Sauer[25].

$$\frac{\partial(\alpha_v\rho_v)}{\partial t}+\frac{\partial(\alpha_v\rho_v u_j)}{\partial x_j}=\dot{m}^+-\dot{m}^- \tag{5}$$

where the source terms $\dot{m}^+$ and $\dot{m}^-$ represent the effects of the evaporation and the condensation during the phase change and they are derived from the bubble dynamics equation for the generalized Rayleigh-Plesset equation. Their definitions are as follows:

$$\dot{m}^+=\frac{\alpha_v(1-\alpha_v)\rho_l\rho_v}{\rho}\frac{3}{R_b}\sqrt{\frac{2}{3}\frac{\max(p_v-p,0)}{\rho_l}} \tag{6}$$

$$\dot{m}^-=\frac{\alpha_v(1-\alpha_v)\rho_l\rho_v}{\rho}\frac{3}{R_b}\sqrt{\frac{2}{3}\frac{\max(p-p_v,0)}{\rho_l}} \tag{7}$$

The bubble radius is related to the vapor volume fraction α_v and the bubble number density N_b as follows

$$R_b=\left(\frac{\alpha_v}{1-\alpha_v}\frac{3}{4\pi}\frac{1}{N_b}\right)^{1/3} \tag{8}$$

Herein, N_b the only parameter which needs to be specified, and we let $N_b=10^3$. The saturated vapor pressure is $p_v=3\,540$ Pa. The model constants are based on the work of Schnerr and Sauer[25]. This cavitation model has been validated by many cases, such as the cavitating flows around a three-dimensional hydrofoil[16, 26-27].

Applying the Favre-filtering operation to Eqs. (1) and (2), the LES equations are obtained as:

$$\frac{\partial\rho}{\partial t}+\frac{\partial(\rho\overline{u}_j)}{\partial x_j}=0 \tag{9}$$

$$\frac{\partial(\rho\overline{u}_i)}{\partial t}+\frac{\partial(\rho\overline{u}_i\overline{u}_j)}{\partial x_j}=-\frac{\partial\overline{p}}{\partial x_i}+\frac{\partial}{\partial x_j}\left(\mu\frac{\partial\overline{u}_i}{\partial x_j}\right)-\frac{\partial\tau_{ij}}{\partial x_j} \tag{10}$$

where the over-bars denote filtered quantities. The non-linear term τ_{ij} in Eq. (10) is called the sub-grid scale (SGS) stress, which is defined as

$$\tau_{ij}=\rho(\overline{u_iu_j}-\overline{u}_i\overline{u}_j) \tag{11}$$

The SGS stress is modeled by the eddy viscosity model, where it is assumed that the SGS stresses are proportional to the modulus of the strain rate tensor, $\overline{S}_{ij}$, of the filtered large-scale flow.

$$\tau_{ij}-\frac{1}{3}\tau_{kk}\delta_{ij}=-2\mu_t\overline{S}_{ij} \tag{12}$$

where τ_{kk} is the isotropic part, $\overline{S}_{ij}$ is the rate-of-strain tensor in the resolved scale, μ_t is the sub-grid scale turbulent viscosity and with the LES wall adapting local eddy-viscosity (WALE) model[28], we have:

$$\mu_t=\rho\Delta_s^2\frac{(S_{ij}^dS_{ij}^d)^{3/2}}{(\overline{S}_{ij}\overline{S}_{ij})^{5/2}+(S_{ij}^dS_{ij}^d)^{5/4}} \tag{13}$$

$$\overline{S}_{ij}=\frac{1}{2}\left(\frac{\partial\overline{u}_i}{\partial x_j}+\frac{\partial\overline{u}_j}{\partial x_i}\right) \tag{14}$$

$$S_{ij}^d=\frac{1}{2}(\overline{g}_{ij}^2+\overline{g}_{ij}^2)-\frac{1}{3}\delta_{ij}\overline{g}_{kk}^2 \tag{15}$$

$$\overline{g}_{ij}=\frac{\partial\overline{u}_i}{\partial x_j} \tag{16}$$

$$\Delta_s=\min(kd,C_sV^{1/3}) \tag{17}$$

where Δ_s is the sub-grid scale mixing length, k is von Karman's constant, d is the distance to the closest wall, V is the volume of the grid cell and $C_s=0.325$ is the WALE constant based on calibrations using freely decaying isotropic homogeneous turbulence[28].

1.2 *Fluid-structure interaction (FSI) technique*

During the fluid-structure interaction (FSI), the flexible structure will deform under the hydrodynamic forces, and the structure deformations will in turn alter the surrounding flows and change the hydrodynamic forces, until a static equilibrium is reached. As the FSI technique is the key issue in the CFD-CSD coupling approach[29], Huang et al.[30] developed a coupling strategy including the Fluid-structure interpolation and the volume mesh motion schemes based on radial basis functions. Their coupling strategy enjoys a good performance in studying the aeroelastic effects on the grid fin aerodynamics in transonic and supersonic regimes. Inspired by their work, a modified fluid-structure technique is proposed in this paper to solve this static hydro-elastic problem by incorporating a user defined function (UDF) code in the commercial software FLUENT, where the hydrodynamic forces and the structural motions are solved separately. The iterative scheme is as follows:

(1) Compute the hydrodynamic forces using the governing equations given in Section 1.1.

(2) Interpolate the forces from the hydrodynamic nodes onto the structural nodes. It is noted that the hydrodynamic nodes are not the same as the structural nodes at the fluid-structure interface. Therefore, according to the physical laws including the conserva-

tion of the total force, torque and energy, it is necessary to realize the transfer of the force and the displacement between the hydrodynamic nodes and the structural nodes by using the radial basis function (RBF) interpolation[30].

(3) Calculate the structural deformation using the flexibility method. The elastic hydrofoil here is represented by a cantilever beam. The natural frequency ω_i and its corresponding normalized shape function $\varphi_i(x)$ are as follows:

$$\omega_i = (\beta_i l)^2 \sqrt{\frac{EI}{\rho_s S l^4}} \quad (i = 1,2,3,\cdots) \tag{18}$$

$$\varphi_i(x) = \cos\beta_i x - \cosh\beta_i x - \theta_i(\sin\beta_i x - \sinh\beta_i x) \tag{19}$$

$$\theta_i = \frac{\cos\beta_i l + \cosh\beta_i l}{\sin\beta_i l + \sinh\beta_i l} \tag{20}$$

where $\beta_1 l = 1.875$, $\beta_2 l = 4.694$, $\beta_3 l = 7.855$. The flexible hydrofoil material properties are given in Table 1. Modulus of elasticity E is 7.375×10^8 Pa, I represents the three-dimensional generalized moment of inertia of the foil along its elastic axis, the structure density ρ_s is 1 480 kg/m^3, Poisson coefficient is 0.35, the foil span l is 0.191 m, the foil section area S is 0.00265 m^2.

(4) Interpolate the deformation from the structural nodes onto the hydrodynamic nodes at the interface and deform the volume grids in the fluid computational domain by using the RBF interpolation method. In order to reduce the computational complexity of the mesh motion and improve the efficiency, the greedy algorithm proposed by Rendall and Allen[31] is adopted to reduce the number of control points, with an adequate accuracy of the deformation at the fluid-structure interface, the maximum interpolation error being in the order of 10^{-3}. The assessment of the RBF interpolation accuracy was made in literature[30].

(5) If the static equilibrium is reached, move to the next time-step, else repeat (1)-(4).

1.3 *Physical and simulation setup*

A NACA66 hydrofoil is used in the present study, with its computational domain as shown in Fig. 1. The hydrofoil has a maximum thickness-to-chord ratio of 12% at the position 45% chord length from the leading edge. The hydrofoil chord length is $C = 0.15$ m, the hydrofoil span length is $l = 0.191$ m, and the angle of attack is 8 degrees. The hydrofoil is fixed in the water tunnel and the test section is $14C$ (length)× $10C$ (height)× $2C$ (width), with the free stream velocity $U_\infty = 5$ m/s yielding a Reynolds number of $Re=\rho U_\infty C/\mu=5.59\times10^7$. The outlet pressure is set according to the cavitation number as $\sigma = (p_\infty - p_v)/(0.5\rho_l U_\infty^2) = 0.8$. Figure 2 shows the three-dimensional fluid mesh. An O-Y type mesh is generated in the computational domain with a sufficient refinement near the hydrofoil surface in order to satisfy the condition that $y^+ = y\mu_\tau/\nu \approx 1$, where y is the distance from the first cell to the hydrofoil surface, μ_τ is the wall frictional velocity. Based on the mesh independence study, the number of the final grid nodes is 3 937 911.

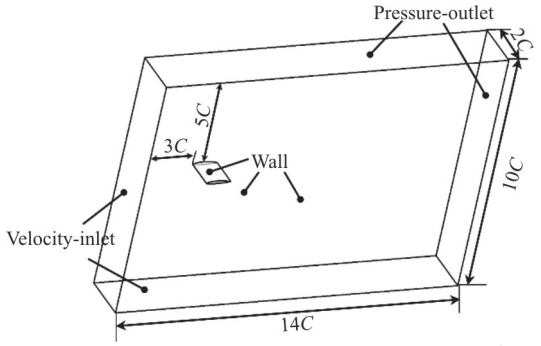

Fig. 1 Computational domain for NACA66

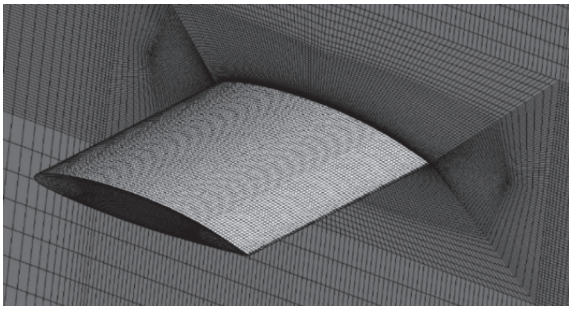

Fig. 2 Fluid mesh grids

Table 1 The parameters of the hydrofoils

Chord length, C /m	Span length, l /m	Maximum thickness-to-chord ratio/%	Foil section area, S /m^2	Distance between the foil tip and the wall/m	Modulus of elasticity, E /Pa	Density, ρ_s /kg·m^{-3}	Poisson coefficient
0.15	0.191	12	0.00265	0.109	7.375×10^8	1 480	0.35

The unsteady governing equations are discretized in both space and time. The second order implicit scheme is used for transient formulations. For the spatial discretization of the convection terms, the PRESTO! scheme is used for the pressure equation, and the second order upwind scheme is used for the other convection-diffusion equations. The SIMPLEC algorithm is used for the pressure-velocity coupling solution, to obtain a converged solution quickly with the under-relaxation factor set to 1.0. The numerical simulation of the unsteady cavitating induced vibrations are started from an unsteady cavitating flow field. Subsequently, the in-house UDF code is compiled and turned on in the dynamic mesh panel. The time step is set to 1×10^{-4} s so that the courant number is about 1.

In order to estimate the accuracy of the present fluid-structure interaction technique, we simulate the fully-wetted hydrofoil in the still water with an initial force and analyze the vibration response by monitoring the vibrations at the hydrofoil tip. On the other hand, the ANSYS workbench commercial software is used to perform the modal analysis incorporated with the acoustic method in order to obtain the first-order mode of the hydrofoil in the water. Figure 3 shows the time dependent displacement at the foil tip. The hydrofoil oscillates periodically and its displacement gradually decreases due to the energy dissipation. In Fig. 4, the calculated natural frequency in the still water is $f_wC/U_\infty=1.17$ by using the present modified FSI technique, and this is the same as predicted by the ANSYS workbench, demonstrating that the modified fluid-structure interaction technique in the present study is reliable.

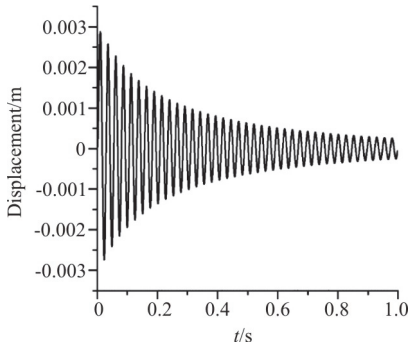

Fig. 3 Predicted vibration displacement in still water by using the modified FSI technique

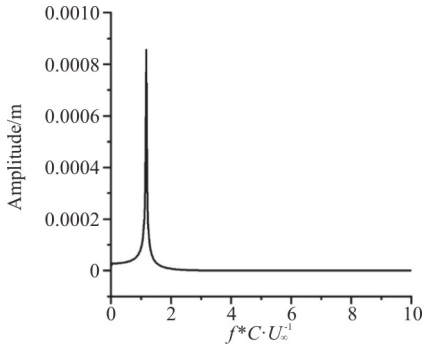

Fig. 4 Predicted natural frequency in still water by using the modified FSI technique $(f_wC/U_\infty=1.17)$

Table 2 Predicted frequencies of flexible hydrofoil in air, still water and cavitating flows

Dry frequency f_dC/U_∞	Fully-wetted frequency f_wC/U_∞	Flow-induced frequency $f_{cs}C/U_\infty$	Cavity shedding frequency $f_{c1}C/U_\infty$
1.47	1.17	0.99	0.51

2. Results and discussions

2.1 *Flow-induced vibration characteristics*

As the vibration characteristics of the flexible hydrofoil, the dry frequency (in the air) is $f_dC/U_\infty=1.47$ and the fully-wetted frequency (in the still water) is $f_wC/U_\infty=1.17$, as shown in Table 2. It is shown that a 20.4% reduction is resulted in the natural frequency due to the added mass in the still water. In the air, the added mass of the air can be ignored, while in the still water, the added mass due to the water must be considered.

In the present work, we mainly focus on the flow-induced vibration characteristics of the flexible hydrofoil, so it is necessary to carry out a preliminary analysis for the rigid hydrofoil around the cavitating flows. Figure 5 shows the frequency spectrum of the vapor volume evolution around the flexible and rigid hydrofoils. The cavity shedding frequency for the

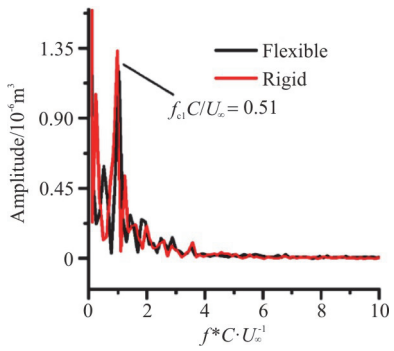

Fig. 5 (Color online) Frequency spectrum of the vapor volume evolution around the flexible hydrofoil and rigid hydrofoil

rigid hydrofoil is $f_{c1}C/U_\infty=0.51$, which is the same as that for the flexible hydrofoil. This demonstrates that the structure vibration is not large enough to

affect the cavitation evolution, so the cavitation around the flexible hydrofoil keeps the same pace as that around the rigid hydrofoil. Since 4 864 samples are taken every 1×10^{-4} s during the unsteady calculations, the frequency resolution of the vapor volume evolution is $f^*C/U_\infty = 0.06$, which could be improved by increasing either the sampling time or the sampling frequency.

For the flexible hydrofoil, the cavitation unsteadiness would cause the vibrations of the flexible structure, as illustrated in Fig. 6. It is shown that the hydrofoil tip vibrates evidently with small amplitudes in the time history. As the first derivative of the vibration displacement, the vibration velocity represents the vibration intensity and the displacement can be visually observed at the hydrofoil tip. The vibration displacement ranges from 0.74 mm to 0.82 mm, and the average displacement is 0.77 mm with the standard deviation of 1.5×10^{-5}. This is in the same order of magnitude as predicted in literature [6, 8, 32-33]. The vibration velocity fluctuates ranging from -9.0×10^{-3} m/s to 9.1×10^{-3} m/s, and the average value is -1.3×10^{-4} m/s with the standard deviation of 3.4×10^{-3}.

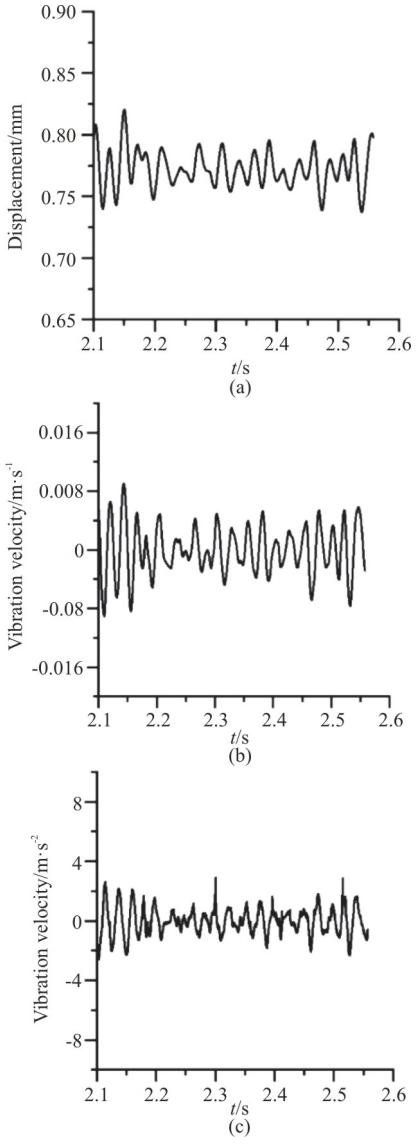

Fig. 6 Time-dependent vibrations of displacement, velocity and acceleration at the flexible hydrofoil tip

To investigate the effect of the cavitation behavior on the flow-induced vibration, the Fast Fourier Transform is carried out for the vibration displacement and the results are analyzed together with the vapor volume oscillations, as shown in Fig. 7. It is found that the dominant flow-induced vibration frequency $f_{cs}C/U_\infty = 0.99$ is approximately twice the cavity shedding frequency. It is observed that the other harmonics due to the cavitation oscillations also make contributions to the responses of the flexible hydrofoil.

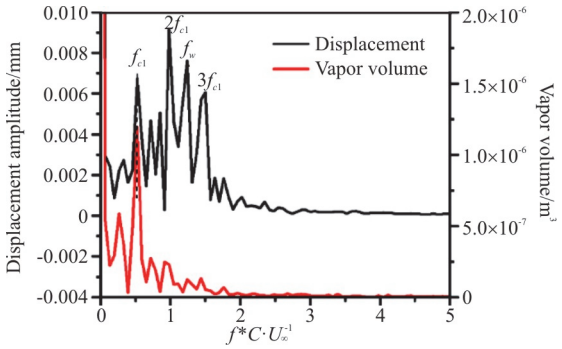

Fig. 7 (Color online) The displacement and vapor volume oscillations of the flexible hydrofoil in cavitating flows

The cavitation evolution is closely associated with changes in the lift coefficient, which is defined as $C_L = \text{lift}/(0.5\rho_l U_\infty^2 Cl)$. Therefore, it is reasonable to analyze the amplitude responses of the lift coefficient along with the cavitation oscillations for the flexible hydrofoil as shown in Fig. 8. The lift coefficient (C_L) fluctuates periodically ranging from 0.43 to 0.53, and the average value is 0.50 with the standard deviation of 0.010. The C_L amplitude is significantly amplified at the cavity shedding frequency.

2.2 *The transient cavitation patterns associated with the flow-induced vibrations*

Figure 9 shows the time-history of the vapor volume and the vibration displacement of the flexible hydrofoil within several cycles. Eight instants in one typical cavitation cycle are selected from Fig. 9 to illustrate the transient cavitating flow patterns around the flexible hydrofoil in Fig. 10 by using the iso-surface of $\alpha_v = 0.1$ overlaid with the streamwise velocity. The two-dimensional contours represent the

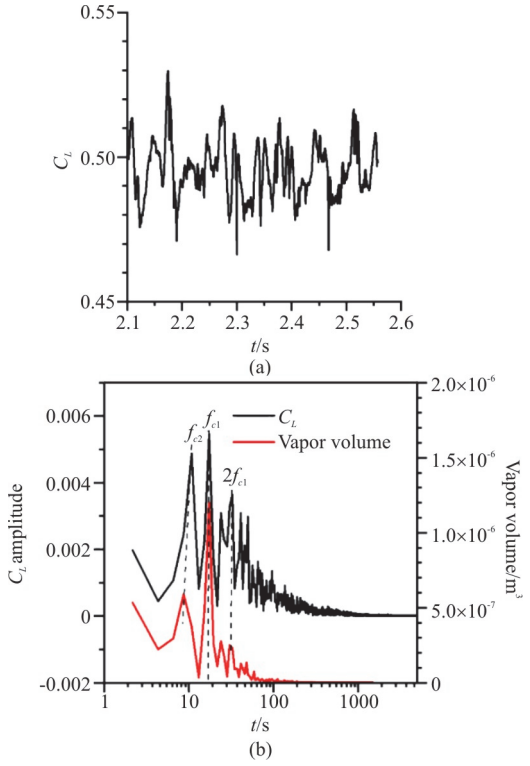

Fig. 8 (Color online) The lift (C_L) and vapor volume oscillations of the flexible hydrofoil in cavitating flows

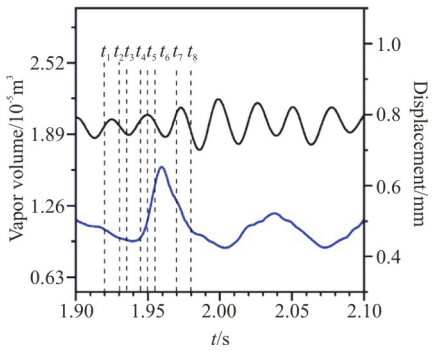

Fig. 9 (Color online) Time-history of the vapor volume and hydrofoil displacement

distributions of the vapor volume fraction at plane I, 60 mm away from the solid wall as shown in Fig. 11.

From t_1 to t_3, the attached cavity is generated from the leading edge and grows on the suction side, meanwhile the cloud cavity continuously moves downstream with the decrease of the cloud cavity volume until it collapses at t_4. It is observed that the cavity rear part begins to oscillate and breaks into small-scale cloud cavities at t_4. The displacement goes up firstly to a maximum and then keeps decreasing to a minimum at t_3. During this process, as shown in Fig. 12, a re-entrant flow develops at the rear of the attached cavity due to the strong adverse pressure gradient and moves toward the leading edge. The re-entrant flow breaks through the liquid-vapor interface and makes the attached cavity detached from the hydrofoil, causing the attached cavity to gradually shrink and break the rear part into the cloud cavities from t_4 to t_7. The displacement goes up from t_3 to t_5, then gradually decreases to a minimum displacement corresponding to the maximum vapor volume and tends to increase until t_7. At $t = t_7$, the attached cavity shrinks to the leading edge with the presence of several medium-scale cloud cavities. Further in this cycle, the cloud cavities continuously move downstream as illustrated at $t = t_8$ and begins to collapse where the pressure is higher than the saturated vapor pressure. At the same time, the cavity starts to grow, followed by a new cycle.

As shown by the cavitation patterns in Fig. 10, the cavitation structures are strongly three-dimensional due to the existence of the gap flow and the solid wall (referring to the root end of the hydrofoil). The sheet cavity near the hydrofoil tip is very stable with a triangular shape due to the gap liquid flow. Besides, there is a rectangular cavity at $t = t_1$ and t_6 - t_8 due to the existence of the low-velocity boundary layer at the solid wall of the hydrofoil root. The strong unsteadiness of the sheet/cloud cavities is mainly observed in the middle of the span, and the unsteady cavitating patterns are close to the hydrofoil root, which indicates that the gap flow has a greater effect on the cavitation behavior than the solid wall of the hydrofoil root.

To investigate the effect of the hydrofoil flexibility on the cavitating flows, the evolutions of the cavitation patterns for the rigid and flexible hydrofoils are compared in Fig. 13. It is observed the cavitation evolutions for the rigid and flexible hydrofoils are similar, including the cavity growth, development, shedding and collapse processes. For the flexible hydrofoil, although the vibration displacement is very small, the cavitation features are more complex during the cavity developing and shedding processes. From Figs. 13(b) and 13(c), it is seen that the cavity trailing edge (CTE) of the flexible hydrofoil is longer than that of the rigid hydrofoil. In the shedding process, the attached cavity around the flexible hydrofoil starts to oscillate and break into small-scale cloud cavities at the cavity rear part, as shown in Figs. 13(d)-13(f), while the cavity around the rigid hydrofoil is much more stable. Subsequently, instead of shedding of the large-scale cloud cavities as shown in Figs. 13(g) and 13(h), the cavity for the flexible hydrofoil breaks into medium-scale cloud cavities and moves downstream. It is found that the cavitation shedding process is closely associated with

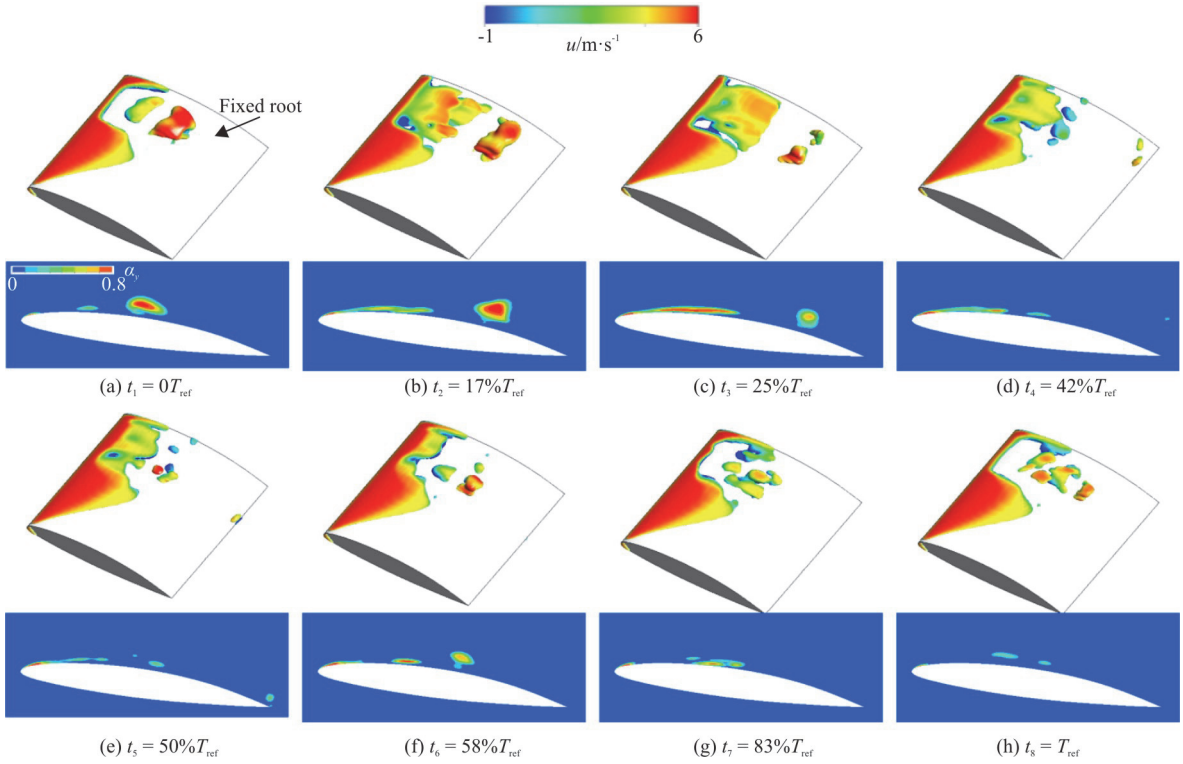

Fig. 10 The variation of the three-dimensional cavitation structures during a typical cycle depicted by the iso-surface of $\alpha_v = 0.1$ overlaid with the streamwise velocity. The two-dimensional contours represent the distributions of the vapor volume fraction at plane I, as shown in Fig. 11

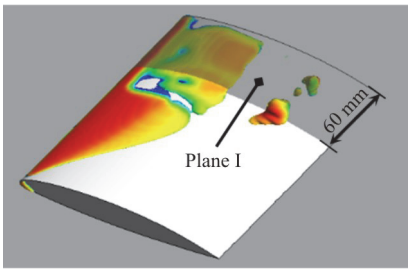

Fig. 11 (Color online) The position of Plane I, 60 mm away from the solid wall

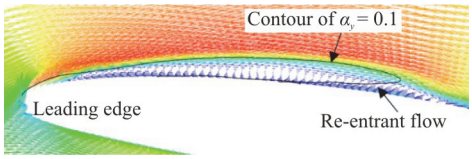

Fig. 12 (Color online) Velocity vectors near the leading edge at $t = 25\%T_{ref}$

the unsteady hydroelastic response, and the cavity rear part appears to be fragmented.

2.3 *Analysis of unsteady vortex structures obtained with different vortex identification methods*

From the above results, the transition of the attached cavity to the cloud cavity is strongly unstable. According to the cavitation-vortex interaction mechanism proposed by Ji et al.[16-17], the cavitation affects the vorticity distribution by the vortex stretching, the vortex dilation and the baroclinic torque terms. Inspired by their work, three vortex identification methods, i.e., the vorticity, the Q- criteria and the Ω method, are adopted to further investigate the unsteady vortex features around the flexible hydrofoil.

According to the Helmholtz velocity decomposition, the velocity gradient tensor $\nabla \boldsymbol{u}$ can be decomposed into the symmetric part $\boldsymbol{A}$ and the anti-symmetric part $\boldsymbol{B}$ as in Eq. (21). Different vortex identification methods are defined based on a general understanding that the symmetric part represents the deformation and the anti-symmetric part represents the rotation. The vorticity is defined as the anti-symmetric tensor of the velocity gradient tensor, i.e., the part $\boldsymbol{B}$ in Eq. (23). In the Q-criterion[19], Q is defined as in Eq. (24), where a and b are the squares of the Frobenius norm of $\boldsymbol{A}$ and $\boldsymbol{B}$ given in Eq. (22). The part with $Q > 0$ defines as the vortex region. Liu et al.[22] proposed a new vortex identification method of Ω given in Eq. (24), which is a ratio of the vortical vorticity over the total vorticity. $\Omega = 0$ represents the pure deformation and $\Omega = 1$ indicates the rigidly rotational flow.

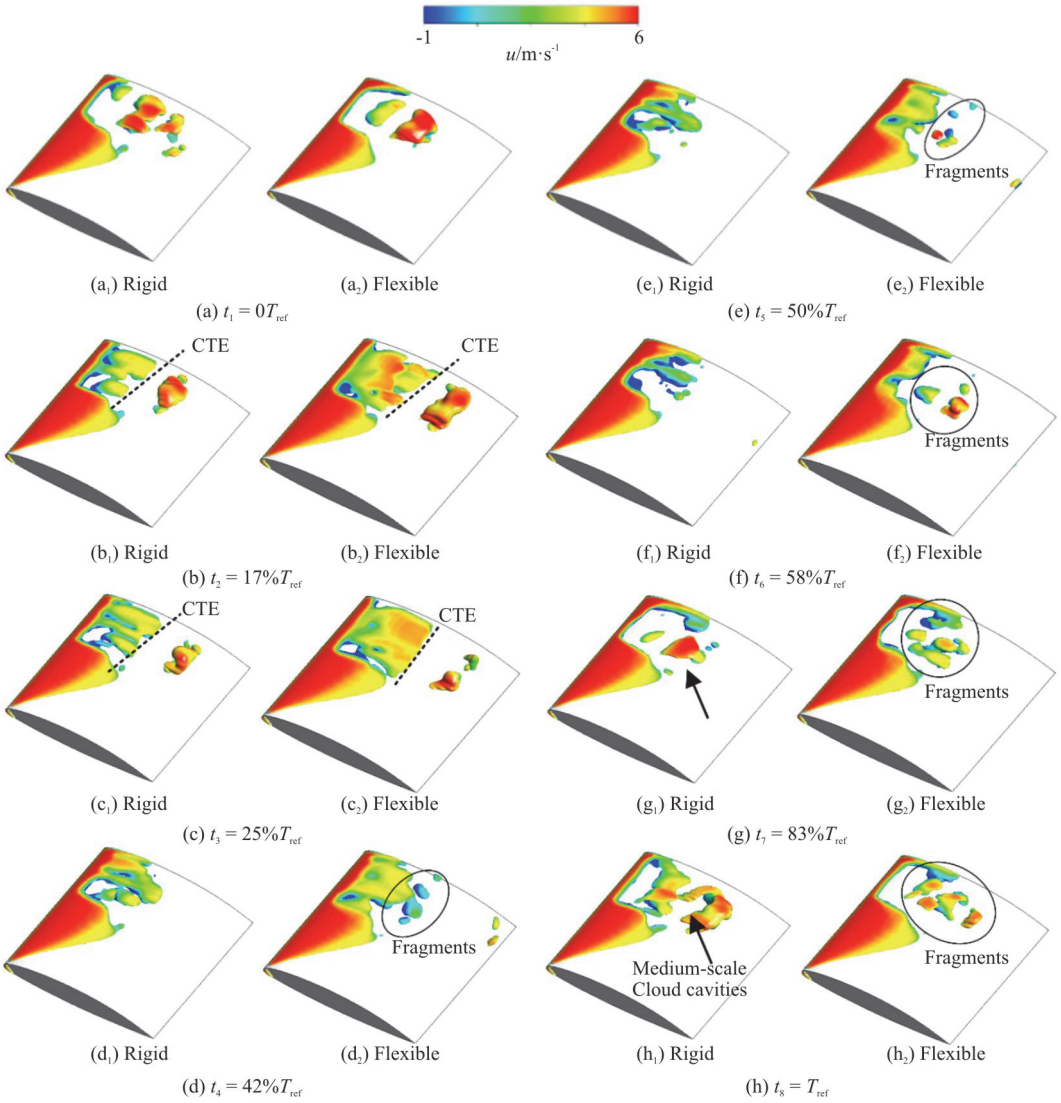

Fig. 13 (Color online) Comparison of cavitation features between the rigid and flexible hydrofoils

ξ is a small positive number used to avoid division by zero and is recommended to take a value in the level of 10^{-3} [34-35].

$$\nabla \boldsymbol{u} = \frac{1}{2}(\nabla \boldsymbol{u} + \nabla \boldsymbol{u}^{\mathrm{T}}) + \frac{1}{2}(\nabla \boldsymbol{u} - \nabla \boldsymbol{u}^{\mathrm{T}}) = \boldsymbol{A} + \boldsymbol{B} \tag{21}$$

$$a = \mathrm{trace}(\boldsymbol{A}^{\mathrm{T}}\boldsymbol{A}), \quad b = \mathrm{trace}(\boldsymbol{B}^{\mathrm{T}}\boldsymbol{B}) \tag{22}$$

$$\text{Vorticity} \quad Z \quad \omega_z = \frac{\partial v}{\partial x} - \frac{\partial u}{\partial y} \tag{23}$$

$$Q \quad \text{criterion} \quad Q = \frac{1}{2}(b - a) \tag{24}$$

$$\Omega \quad \text{method} \quad \Omega = \frac{b}{a + b + \xi} \tag{25}$$

To have a further insight into the cavitation-vortex interaction, Fig. 14 shows the relation between the cavitation and the vortex evolution. Since b in Eq. (22) represents the vortical vorticity, it can be treated as the vortex strength in this paper, which is also thus selected by Zhang et al.[36]. It is observed that the variation trend of the cavity is consistent with that of the vortex.

Figure 15 depicts the vapor volume fraction distribution and the contours of the vorticity, the Q-criteria and the Ω method on the plane I. These results are used to (1) evaluate the capability of different vortex identification methods, (2) analyze the effect of the cavitation evolution on the vortex structures.

For $t = 17\%T_{\mathrm{ref}}$, the attached cavity develops along the suction surface with the cloud cavity transporting downstream. The cavity interface is represented by the black line with the contour line of $\alpha_v = 0.1$. The vorticity (ω_z) on the plane I concentrates around the foil surface with negative values

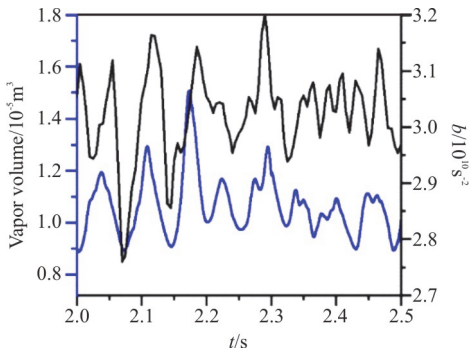

Fig. 14 (Color online) Time-dependent vapor volume and vortex strength represented by b

on the suction surface and positive values on the pressure surface. Negative vorticity means the clockwise rotation and positive vorticity means the counter-clockwise rotation. The clockwise vortex is mainly located in the sheet cavity region, and a strip counter-clockwise vortex is observed on the foil pressure surface. A vortex pair is observed in the foil trailing. Both the Q- criteria and the Ω method identify strong vortices in the sheet/cloud cavitation region and weak vortices in the foil trailing edge region and the foil wake flow region. The differences are (1) the Ω method identified vortices mainly locate outside the cavity interface and strong vortices are observed in the foil wake flows, while (2) the Q- criteria identifies vortices inside and outside the sheet cavity with weak vortices in the foil wake flows. The large-scale vortex structures are identified by experiments in the cavity sheet rear part and in the wake region[37-38]. Therefore, it is shown that the Q- criteria and the Ω method can identify vortices in the cavity region very well but identify vortices in the foil wake with different positions and magnitudes.

In the shrinkage stage ($t = 50\%T_{\text{ref}}$), a re-entrant jet flow is observed beneath the attached cavity and it causes the cavity oscillate in the rear part and break into small-scale cloud cavities. With the vorticity identification, the vortex structures are shown to be distributed around the foil surface in the clockwise direction in the re-entrant jet region and in the counter-clockwise direction in the cavity region. There is also a positive strip vortex on the pressure surface and a vortex pair near the foil trailing edge. Both the Q- criteria and the Ω method can identify the vortex structures in the cavitation region and near the foil trailing edge. The Q- criteria not only can identify cavity-interface-like vortices which are easily distinguished by the Ω method but also can identify vortices inside the sheet cavity region. In contrast, strong vortices in the foil wake flow are identified by the Ω method.

At $t = T_{\text{ref}}$, the cloud cavity is shedding, moving downstream and the sheet cavity starts to develop again. The vorticity method identifies clockwise vortices near the suction surface and counter-clockwise vortices with a strip shape on the pressure surface. A vortex pair is identified by the ω_z method at the foil trailing edge. The vortex structures in the cavitation region and near the foil trailing edge are visualized by both the Q- criteria and the Ω method, but vortices in the wake flow can only be clearly identified by the Ω method.

From these results, it is seen that the vortices identified by the vorticity method are varied in the transient cavitation evolution due to the strong vortex-cavitation interaction, which is extensively studied by Ji et al.[17]. It is noted that the vorticity shows similar distributions, that is, the clockwise vorticity near the suction surface and counter-clockwise vorticity with a strip shape on the pressure surface. The vortex structures identified by the Q- criteria and the Ω method are distributed in the cavitation region and near the foil trailing edge, especially at the cavity-liquid interface. Due to the downstream transportation of the shedding cavities, the vortices increase and become intensely unstable which can only be identified by the Ω method.

This is clearly illustrated in Fig. 16, where the three-dimensional vortex structures are visualized by the Q- criteria and the Ω method with different thresholds at $t = 50\%T_{\text{ref}}$. It is observed that both methods can identify the vortex ring at the foil trailing edge and the tip-leakage vortex at the foil tip although with different thresholds. However, from Figs. 16(a) and 16(b), the vortex structures in the attached cavity region are more sensitive to the thresholds of the Ω method, that is, the Ω thresholds mainly affect the vortex visualization in the attached cavitation region. In contrast, the thresholds of the Q- criteria have major effects on the vortex identification in the wake flows as shown in Figs. 16(c) and 16(d).

Furthermore, the vortex strength is analyzed quantitatively. Based on the vortex structures identified by the iso-surface of $\Omega = 0.52$ in Fig. 16(a) and the iso-surface of $Q = 200\ \text{s}^{-2}$ in Fig. 16(b), we have 121 122 points in the Ω vortex and 109 463 points in the Q vortex. Figure 17 shows the vortex strength (b) distributions of the two vortex structures at $t = 50\%T_{\text{ref}}$, where the horizontal axis is scaled by taking twice lg10 of the b values in order to clearly display the b distributions. The Ω method can identify vortices in regions I and II while

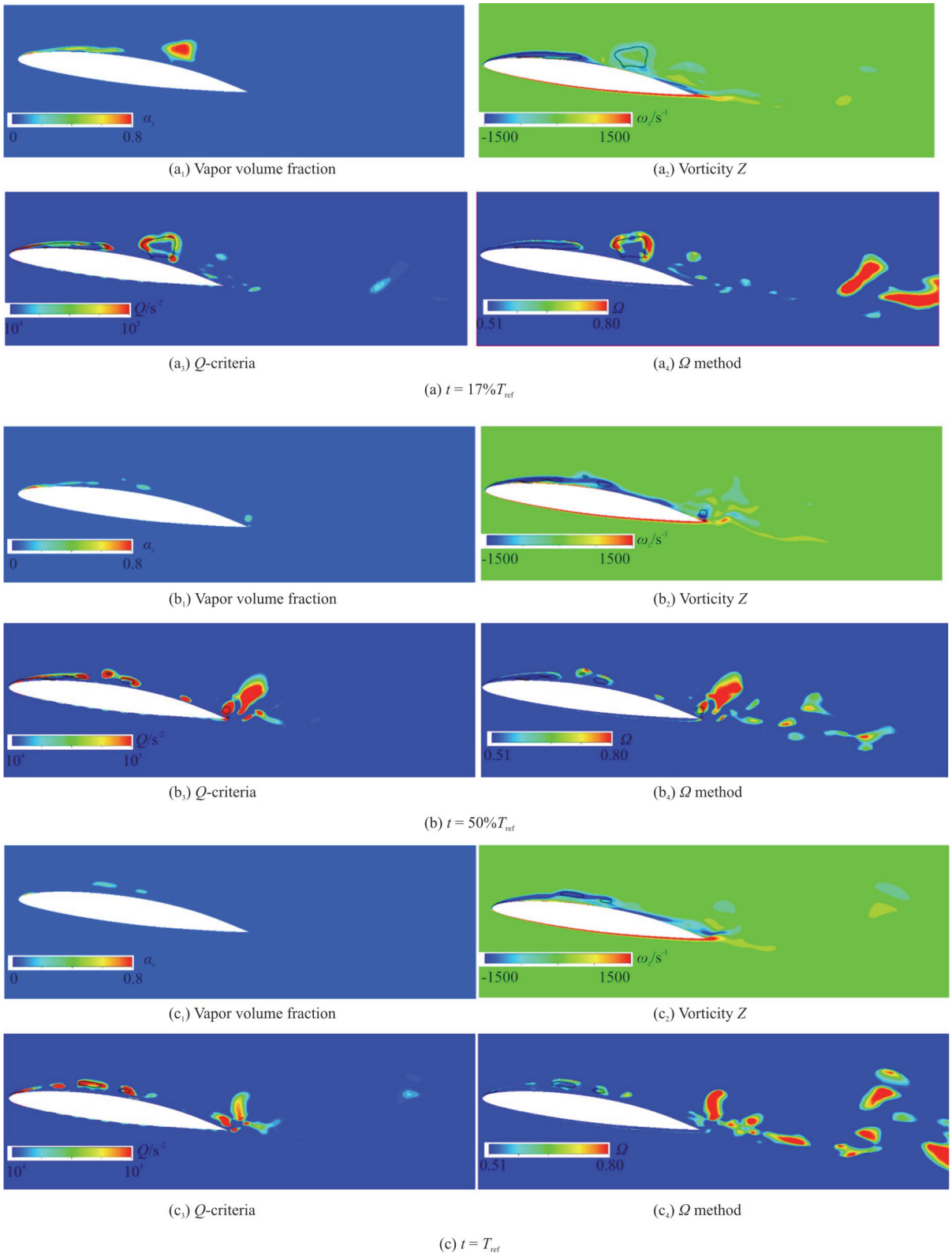

(a_1) Vapor volume fraction

(a_2) Vorticity Z

(a_3) Q-criteria

(a_4) Ω method

(a) $t = 17\%T_{ref}$

(b_1) Vapor volume fraction

(b_2) Vorticity Z

(b_3) Q-criteria

(b_4) Ω method

(b) $t = 50\%T_{ref}$

(c_1) Vapor volume fraction

(c_2) Vorticity Z

(c_3) Q-criteria

(c_4) Ω method

(c) $t = T_{ref}$

Fig. 15 (Color online) Distributions of the vapor volume fraction (α_v) and vortex visualization with vorticity, Q- criteria and Ω method at three instants. The black line represents the contour line of $\alpha_v = 0.1$

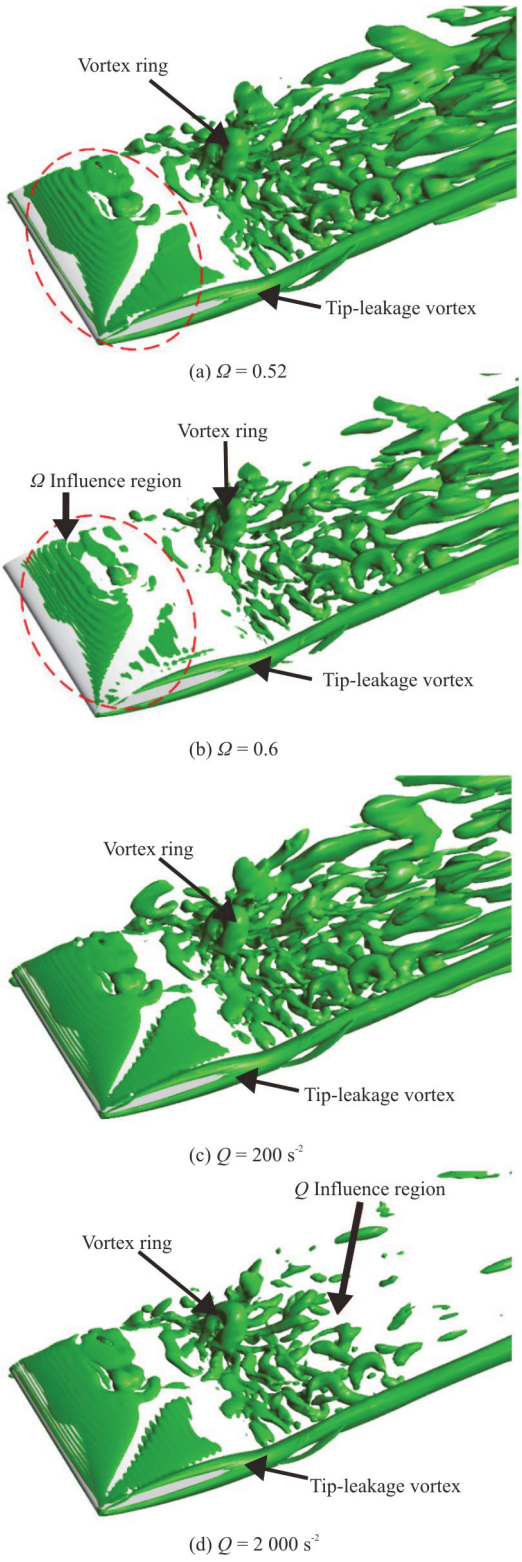

Fig. 16 (Color online) Three-dimensional vortex visualizations using Q- criteria and Ω method at $t = 50\%T_{\text{ref}}$

the Q- criteria can only identify vortices in region III. Note that in regions II and III large b values mean strong vortices and in region I small b values mean

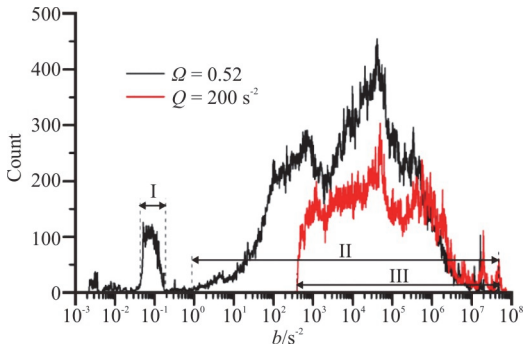

Fig. 17 (Color online) The statistical distribution of the vortex regions identified by the $Q = 200\,\text{s}^{-2}$ and $\Omega = 0.52$ at $t = 50\%T_{\text{ref}}$ indicating that Ω method can identify all scales of vortices including strong and weak vortices and Q- criteria can identify strong vortices

weak vortices. Therefore, it is demonstrated that the Ω method can identify all scales of vortices including strong and weak vortices and the Q- criteria prefers to identify strong vortices.

3. Conclusions

In this paper, numerical simulations of the unsteady cavitating flows around a flexible NACA66 hydrofoil are carried out by using the modified partitioned FSI approach. The modi- fied coupling strategy includes: (1) the hydrodynamic solution using a LES together with a homogenous cavitation model, (2) the structural deformation solved as for a cantilever beam, (3) fluid-structural interpolation and volume mesh motion based on the radial basis functions and greedy algorithm. The flow-induced vibration characteristics together with the transient cavitation behaviors are investigated. Furthermore, the unsteady vortex features due to the hydroelastic response are analyzed by using three vortex identification methods (vorticity, Q- criteria and Ω method). Several observations are as follows:

(1) The dominant flow-induced vibration frequency is twice the cavity shedding frequency. Note that the cavity shedding frequency is the same for the rigid and flexible hydrofoils, demonstrating that the structure vibration is not large enough to affect the cavitation evolution.

(2) The predicted cavitating behaviors are strongly three-dimensional, that is, the cavity is (a) in a triangular shape near the hydrofoil tip, (b) in a rectangular shape near the hydrofoil root, and (c) with a strong unsteadiness in the middle of the span, including the attached cavity growth, oscillation and shrinkage, break-off and collapse downstream. The

unsteady hydroelastic response will affect the cavitation shedding process with small-scale fragments at the cavity rear part.

(3) For the flexible hydrofoil, the cavity variation trend is consistent with the vortex evolution. The vortex structures are distributed near the foil trailing edge and in the cavitation region, especially at the cavity-liquid interface. With the transporting downstream the shedding cavities, the vortices gradually increase in the wake flows.

(4) Regarding to the vortex identification methods, both the Q-criteria and the Ω method can identify the vortex structures near the foil trailing edge and in the cavitation region. The Ω method can visualize the vortex increase in the wake flows with the transporting downstream the shedding cavities. Besides, the Ω method can identify all scales of vortices including strong and weak vortices and the Q-criteria prefers to identify strong vortices.

It is noted that the elastic hydrofoil is solved as a cantilever beam in this paper without considering the effect of twist on the cavity behaviors. The twist deformation is also very important for the pressure distribution and the structural displacement, and this can be incorporated into the present FSI technique based on the three-dimensional structural modes.

References

[1] Brennen C. E. Cavitation and bubble dynamics [M]. Cambridge, UK: Cambridge University Press, 2014.

[2] Huang B., Qiu S. C., Li X. B. et al. A review of transient flow structure and unsteady mechanism of cavitating flow [J]. *Journal of Hydrodynamics*, 2019, 31(3): 429-444.

[3] Arndt R. E. A. Cavitation in fluid machinery and hydraulic structures [J]. *Annual Review of Fluid Mechanics*, 1981, 13: 273-326.

[4] Luo X. W., Ji B., Tsujimoto Y. A review of cavitation in hydraulic machinery [J]. *Journal of Hydrodynamics*, 2016, 28(3): 335-358.

[5] Smith S. M., Venning J. A., Giosio D. R. et al. Cloud cavitation behavior on a hydrofoil due to fluid-structure interaction [J]. *Journal of Fluids Engineering*, 2019, 141(4): 041105.

[6] Wu Q., Wang C. C., Huang B. et al. Measurement and prediction of cavitating flow-induced vibrations [J]. *Journal of Hydrodynamics*, 2018, 30(6): 1064-1071.

[7] Ducoin A., Astolfi J. A., Sigrist J. F. An experimental analysis of fluid structure interaction on a flexible hydrofoil in various flow regimes including cavitating flow [J]. *European Journal of Mechanics-B/Fluids*, 2012, 36: 63-74.

[8] Wu Q., Huang B., Wang G. et al. The transient characteristics of cloud cavitating flow over a flexible hydrofoil [J]. *International Journal of Multiphase Flow*, 2018, 99: 162-173.

[9] Chae E. J., Akcabay D. T., Lelong A. et al. Numerical and experimental investigation of natural flow-induced vibrations of flexible hydrofoils [J]. *Physics of Fluids*, 2016, 28(7): 075102.

[10] Zeng Y. S., Yao Z. F., Zhou P. J. et al. Numerical investigation into the effect of the trailing edge shape on added mass and hydrodynamic damping for a hydrofoil [J]. *Journal of Fluids and Structures*, 2019, 88: 167-184.

[11] Amromin E., Kovinskaya S. Vibration of cavitating elastic wing in a periodically perturbed flow: Excitation of subharmonics [J]. *Journal of Fluids and Structures*, 2000, 14(5): 735-751.

[12] Wu Q., Wang Y., Wang G. Experimental investigation of cavitating flow-induced vibration of hydrofoils [J]. *Ocean Engineering*, 2017, 144: 50-60.

[13] De La Torre O., Escaler X., Egusquiza E. et al. Experimental investigation of added mass effects on a hydrofoil under cavitation conditions [J]. *Journal of Fluids and Structures*, 2013, 39: 173-187.

[14] Ausoni P., Farhat M., Escaler X. et al. Cavitation influence on von Kármán vortex shedding and induced hydrofoil vibrations [J]. *Journal of Fluids Engineering*, 2007, 129(8): 966-973.

[15] So R. M. C., Zhou Y., Liu M. H. Free vibrations of an elastic cylinder in a cross flow and their effects on the near wake [J]. *Experiments in Fluids*, 2000, 29(2): 130-144.

[16] Ji B., Luo X. W., Arndt R. E. A. et al. Large eddy simulation and theoretical investigations of the transient cavitating vortical flow structure around a NACA66 hydrofoil [J]. *International Journal of Multiphase Flow*, 2015, 68: 121-134.

[17] Ji B., Luo X., Arndt R. E. A. et al. Numerical simulation of three dimensional cavitation shedding dynamics with special emphasis on cavitation–vortex interaction [J]. *Ocean Engineering*, 2014, 87: 64-77.

[18] Jeong J., Hussain F. On the identification of a vortex [J]. *Journal of Fluid Mechanics*, 1995, 285: 69-94.

[19] Hunt J. C. R., Wray A. A., Moin P. Eddies, streams, and convergence zones in turbulent flows [R]. Proceedings of the Summer Program. Center for Turbulence Research Report CTR-S88, 1988, 193-208.

[20] Long X., Cheng H., Ji B. et al. Large eddy simulation and Euler–Lagrangian coupling investigation of the transient cavitating turbulent flow around a twisted hydrofoil [J]. *International Journal of Multiphase Flow*, 2018, 100: 41-56.

[21] Tseng C. C., Liu P. B. Dynamic behaviors of the turbulent cavitating flows based on the Eulerian and Lagrangian viewpoints [J]. *International Journal of Heat and Mass Transfer*, 2016, 102: 479-500.

[22] Liu C., Wang Y. Q., Yang Y. et al. New omega vortex identification method [J]. *Science China Physics, Mechanics and Astronomy*, 2016, 59(8): 684711.

[23] Zhang Y. N., Qiu X., Chen F. P. et al. A selected review of vortex identification methods with applications [J]. *Journal of Hydrodynamics*, 2018, 30(5): 767-779.

[24] Wang C. C., Liu Y., Chen J. et al. Cavitation vortex dynamics of unsteady sheet/cloud cavitating flows with shock wave using different vortex identification methods [J]. *Journal of Hydrodynamics*, 2019, 31(3): 475-494.

[25] Schnerr G. H., Sauer J. Physical and numerical modeling of unsteady cavitation dynamics [C]. *Fourth International Conference on Multiphase Flow*, New Orleans, USA, 2001.

[26] Ji B., Long Y., Long X. P. et al. Large eddy simulation of turbulent attached cavitating flow with special emphasis on large scale structures of the hydrofoil wake and turbulence-cavitation interactions [J]. *Journal of Hydrodynamics*, 2017, 29(1): 27-39.

[27] Li D. Q., Grekula M., Lindell P. Towards numerical prediction of unsteady sheet cavitation on hydrofoils [J]. *Journal of Hydrodynamics*, 2010, 22(5Suppl.): 699-704.
[28] Nicoud F., Ducros F. Subgrid-scale stress modelling based on the square of the velocity gradient tensor [J]. *Flow, turbulence and Combustion,* 1999, 62(3): 183-200.
[29] Liu W., Huang C. D., Yang G. W. Time efficient aeroelastic simulations based on radial basis functions [J]. *Journal of Computational Physics*, 2017, 330: 810-827.
[30] Huang C., Liu W., Yang G. Numerical studies of static aeroelastic effects on grid fin aerodynamic performances [J]. *Chinese Journal of Aeronautics*, 2017, 30(4): 1300-1314.
[31] Rendall T. C. S., Allen C. B. Efficient mesh motion using radial basis functions with data reduction algorithms [J]. *Journal of Computational Physics*, 2009, 228(17): 6231-6249.
[32] Meng L., Liu Y., Huang B. et al. Investigation of flow-induced vibration characteristics of flexible hydrofoil in unsteady cavitation [J]. *Engineering Mechanics*, 2017, 34(8): 232-240(in Chinese).
[33] Gao Y. Investigation on flow-induced vibration characteristics of flexible hydrofoil in unsteady cavitating flow [D]. Beijing, China: Beijing Institute of Technology, 2016(in Chinese).
[34] Dong X. R., Wang Y. Q., Chen X. P. et al. Determination of epsilon for Omega vortex identification method [J]. *Journal of Hydrodynamics*, 2018, 30(4): 541-548.
[35] Liu C., Gao Y. S., Dong X. R. et al. Third generation of vortex identification methods: Omega and Liutex/Rortex based systems [J]. *Journal of Hydrodynamics*, 2019, 31(2): 205-223.
[36] Zhang Y. N., Wang X. Y., Zhang Y. N. Comparisons and analyses of vortex identification between Omega method and *Q* criterion [J]. *Journal of Hydrodynamics*, 2019, 31(2): 224-230.
[37] Wosnik M., Arndt R. E. A., Ain Q. Identification of large scale structures in the wake of cavitating hydrofoils using LES and time-resolved PIV [C]. *Proceedings of the 26th Symposium on Naval Hydrodynamics*, Rome, Italy, 2006.
[38] Gopalan S., Katz J. Flow structure and modeling issues in the closure region of attached cavitation [J]. *Physics of Fluids*, 2000, 12(4): 895-911.